nn-2016-082322-revised, 1/2017

An Enzyme-Free Signal Amplification Technique for Ultrasensitive Colorimetric Assay of Disease Biomarkers

Haihang Ye,[†,#] Kuikun Yang,[‡,#] Jing Tao,[ǁ] Yijing Liu,[‡] Qian Zhang,[‡] Sanaz Habibi,[§] Zhihong Nie,[‡,*] and Xiaohu Xia[†,*]

[†]*Department of Chemistry, Michigan Technological University, Houghton, Michigan 49931, United States;*
[‡]*Department of Chemistry and Biochemistry, University of Maryland, College Park, Maryland 20892, United States;*
[ǁ]*Condensed Matter Physics & Materials Science Department, Brookhaven National Laboratory, Upton, New York 11973, United States;*
[§]*Department of Chemical Engineering, Michigan Technological University, Houghton, Michigan 49931, United States.*

[*]Corresponding author. E-mail: xiaxh@mtu.edu (X.X.) and znie@umd.edu (Z.N.)

[#]These two authors contributed equally to this work.

Abstract

Enzyme-based colorimetric assays have been widely used in research labs and clinical diagnosis for decades. Nevertheless, as constrained by the performance of enzymes, their detection sensitivity has not been substantially improved in recent years, which inhibits many critical applications such as early detection of cancers. In this work, we demonstrate an enzyme-free signal amplification technique, based on gold vesicles encapsulated with Pd-Ir nanoparticles as peroxidase mimics, for colorimetric assay of disease biomarkers with significantly enhanced sensitivity. This technique overcomes the intrinsic limitations of enzymes, thanks to the superior catalytic efficiency of peroxidase mimics and the efficient loading and release of these mimics. Using human prostate surface antigen as a model biomarker, we demonstrated that the enzyme-free assay could reach a limit of detection at the femtogram/mL level, which is over 10^3-fold lower than that of conventional enzyme-based assay when the same antibodies and similar procedure were used.

Table of Contents

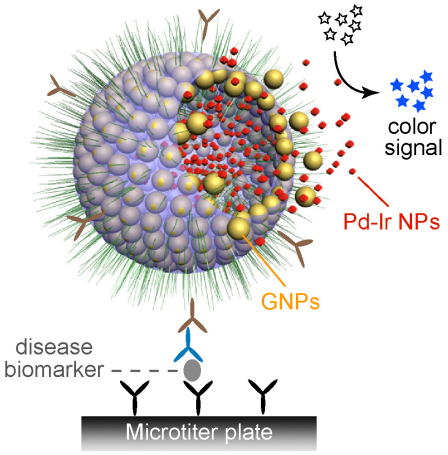

Keywords: iridium nanoparticles · gold vesicle · enzyme mimic · detection · biomarker

Simple and affordable technologies for detection of disease biomarkers are essential to the improvement of standard of living, especially for resource-constrained areas or countries. Enzyme-based colorimetric assays [*e.g.*, enzyme-linked immunosorbent assay (ELISA), immunohistochemistry, and western blot] are broadly recognized as such kind of technology because they can be performed by less-trained personnel with an inexpensive spectrophotometer, ordinary light microscope, or even naked eyes.[1-5] Nevertheless, the major drawback for these colorimetric assays is the relatively low detection sensitivity compared to other technologies such as those based on fluorescence and plasmonics.[6-9]

In conventional colorimetric assays, the detectable color signal is generated from enzymes (in many cases, horseradish peroxidase, HRP) which are conjugated to antibodies and specifically convert substrates to colored molecules.[1-5] Therefore, their detection sensitivity is largely determined by the performance of enzymes. Accordingly, a general strategy for enhancing the sensitivity is to amplify color signal by assembling as many enzyme molecules as possible on certain carriers (*e.g.*, avidin, polymers, and nanoparticles).[10-16] For example, Merkoçi *et al.* conjugated HRPs to gold nanoparticles (GNPs) as carriers and applied these conjugates as labels to ELISA of breast cancer biomarker, of which detection sensitivity was several times higher than conventional ELISA using HRP as label.[14] Qian *et al.* further increased HRP loading amount by employing a combination of GNPs and graphene oxide sheets as carriers, achieving a 64-fold improvement of sensitivity.[15] Despite these demonstrations, the detection sensitivity is ultimately limited by the catalytic efficiency of enzymes and the loading amount of enzymes on a carrier.

Herein, we report an enzyme-free signal amplification technique to break the intrinsic limitations of enzymes, achieving substantially enhanced detection sensitivity. In this technique, sub-10 nm Pd-Ir nanoparticles (NPs) encapsulated gold vesicles (referred to as "Pd-Ir NPs@GVs") are employed as alternatives to enzymes. In this study, we used ELISA as a model platform to demonstrate the enzyme-free technique, because ELISA has been the gold standard for detection and quantification of protein biomarkers for decades.[2] As shown in Figure 1, at elevated temperature, gold vesicles (GVs) captured by analytes liberate thousands of individual Pd-Ir NPs because of the heat-induced breakup of the GV membrane.[17-19] The released Pd-Ir NPs act as peroxidase mimics and generate intense color signal by catalyzing the oxidation of 3,3',5,5'-tetramethylbenzidine (TMB, a classic HRP substrate) by H_2O_2.[20] It should be pointed

out that we have recently demonstrated the peroxidase-like property of Pd-Ir NPs and controlled release of GVs.[17-20] However, to date, there has been no report yet on the development of a signal amplification platform based on the combination of these two systems. The ultralow detection limit of this enzyme-free ELISA arises from the following distinctive features of the amplification technique: *i*) Pd-Ir NPs as enzyme mimics possess much higher catalytic efficiency than natural enzymes, providing enhanced color signal; *ii*) the loading capacity of enzyme mimics is maximized by taking advantage of the large interior 3D space of the GVs as carriers.[21,22] In contrast, the loading of enzymes on carriers in current designs of ELISA is limited by the surface area that allows for the conjugation of enzymes; *iii*) the loading of label-free enzyme mimics of Pd-Ir NPs in the pocket of GVs avoids the loss of catalytic efficiency caused by chemical conjugation; *iv*) Pd-Ir NPs could disperse in catalytic reaction solution upon release, making them more active than immobilized catalysts on solid surfaces, which is the case for conventional ELISAs.

In addition to the high detection sensitivity, our enzyme-free ELISA is featured by good stability and simplicity. The Pd-Ir NPs@GVs are mainly made of inert noble metals with excellent stabilities, enabling them to survive harsh environments. In particular, we have demonstrated in our recent work that the peroxidase-like activity of Pd-Ir NPs was well retained at high temperature (up to 200 ^{o}C) and in strong acidic/basic conditions.[20] In this regard, our platform is more suitable for detection at some extreme conditions compared to natural enzyme-based amplification techniques even though their detection sensitivities may be comparable.[23] As shown in Figure 1, the principle of our enzyme-free ELISA is essentially the same as the conventional HRP-based colorimetric ELISA except for the substitution of HRP with Pd-Ir NPs@GVs. The adoption of existing ELISA platform ensures the simplicity of the assay without the involvement of additional materials and equipment other than the Pd-Ir NPs@GVs. In contrast, other enzyme-free signal amplification systems (*e.g.*, those based on quantum dots[24,25]) may require special materials and/or equipment.

RESULTS AND DISCUSSION

Synthesis and Characterization of Pd-Ir NPs. We started with the synthesis of Pd-Ir NPs by coating an ultrathin layer of Ir on preformed sub-10 nm Pd seeds. In a standard synthesis, a solution of Na_3IrCl_6 was injected slowly into a mixture containing Pd truncated octahedra with

an average size of 5.6 nm as the seeds (Figure S1), L-ascorbic acid as a reductant, and poly(vinyl pyrrolidone) as a colloidal stabilizer (see Supporting Information for details). Figure 2a, b show typical transmission electron microscopy (TEM) images of the produced Pd-Ir NPs. The Pd-Ir NPs exhibit a high purity (>95%) and good uniformity (Figures 2a and S2). A close inspection of the NPs shows that the Pd seeds retained their truncated octahedral shape after the deposition of Ir, indicating a conformal coating of Ir (Figure 2b). The average size of the Pd-Ir NPs was measured to be 6.1 nm, which was 0.5 nm greater than that of the initial Pd seeds. Therefore, the average thickness of the deposited Ir shells was about 0.25 nm, indicating an approximate monolayer coating of Ir on Pd(111) surfaces.[26,27] The molar ratio of Ir to Pd for these Pd-Ir NPs was measured to be 0.28:1 by inductively coupled plasma-optical emission spectrometry (ICP-OES). Based on this data, the morphology of Pd seeds, and the unit cell parameters of Ir,[22] the average number of Ir atomic layers was estimated to be 1 for the Pd-Ir NPs, further confirming the overall monolayer coating of Ir. We also characterized the structure and composition of the Pd-Ir NPs by X-ray diffraction (XRD), high-resolution TEM (HRTEM), high-angle annular dark-field scanning TEM (HAADF-STEM), energy-dispersive X-ray (EDX) mapping/scanning, and X-ray photoelectron spectroscopy (XPS). The XRD patterns of initial Pd seeds and Pd-Ir NPs were shown in Figure S3. It can be seen that the peaks for Pd-Ir NPs were broadened and slightly shifted to the standard face-centered cubic (*fcc*) Ir peak positions as compared to the peaks for *fcc* Pd seeds, suggesting the successful deposition of Ir on Pd seeds and the retention of *fcc* crystal structure for the final Pd-Ir NPs. The typical HRTEM image of an individual Pd-Ir NP reveals the continuous lattice fringes from Pd core to Ir shell, indicating an epitaxial relationship between these two metals (Figure 2c).[28] The color difference between the core (green = Pd) and the shell (red = Ir) of an individual Pd-Ir NP in the EDX maps (Figure 2d) confirmed the Pd-Ir core-shell structures of the final products. The line-scan EDX profile shown in along a corner-to-edge direction of an individual Pd-Ir NP (see Figure S4) verified that the corners and edges were dominated by Ir, whereas the core was made of pure Pd. In addition, XPS was used to identify the oxidation state of the Ir layers. The XPS survey spectrum of the Pd-Ir NPs clearly showed the appearance of Ir 4f peaks (Figure S5a) as compared to the initial Pd seeds, confirming the existence of Ir layers on the Pd cores. The high-resolution spectra of the Ir 4f peaks (Figure S5b) revealed two chemical states for Ir species: *i*) Ir^0 4f7/2 and 4f5/2 peaks at 60.24 and 63.23 eV, and *ii*) Ir^{x+} 4f7/2 and 4f5/2 at 61.25 and 64.46 eV, where the Ir^0 was

dominant. This data suggests that the shell of the Pd-Ir NPs is mainly composed of Ir(0).

Peroxidase-like Activity of Pd-Ir NPs. We quantitatively evaluated the peroxidase-like activity of as-synthesized Pd-Ir NPs by apparent steady-state kinetic assay (see Supporting Information and Figure S6 for details).[20,29] Oxidation of TMB by H_2O_2 was chosen as a model catalytic reaction. The catalytic efficiency, in terms of catalytic constant (K_{cat}, which measures the maximum number of colored products generated per enzyme/mimic per second), for the Pd-Ir NPs was measured to be 1.1×10^5 s^{-1} (Table S1). In comparison, the values of K_{cat} for initial Pd seeds and HRP[29] were 4.8×10^3 and 4.0×10^3 s^{-1}, respectively. This data suggests that *i*) The Pd-Ir NPs are ~28 times more efficient than HRP in generating color products (*i.e.*, oxidized TMB with maximum absorbance at 653 nm[30,31]); and *ii*) the enhanced catalytic efficiency for Pd-Ir NPs was ascribed to the coating of Ir monolayer on Pd seeds.

Encapsulation of Pd-Ir NPs to GVs. We then encapsulated the Pd-Ir NPs into GVs that were achieved by assembling block copolymers (BCPs)-tethered GNPs in an aqueous suspension of Pd-Ir NPs. GNPs with a diameter of 33.0±4.7 nm were first modified with thiol-terminated BCPs of poly(ethylene oxide)-*b*-polystyrene (PEO_{45}-*b*-PS_{260}-SH, Figure S7a) and poly(acrylic acid)-*b*-polystyrene (PAA_{23}-*b*-PS_{250}-SH, Figure S7b) at a molar ratio of 20:1.[32] It should be mentioned that we chose these GNPs of ~33 nm for the assemble of vesicles mainly because *i*) the ease in the functionalization of GNPs with polymers *via* Au-S bond, in order to trigger the formation of GVs and to conjugate biological moieties for sensing; *ii*) the good stability of resultant GVs and their capability in retaining molecules (or nanoparticles) without noticeable leakage for a long time. Our previous studies showed that GVs remain stable for months and minimal leakage of small organic molecules (or drugs) was observed from GVs after weeks, presumably owing to the jamming of particles in the vesicular membranes.[19,33] In contrast, small molecules tend to leak out from liposomes or polymersomes within a few hours, which makes them less attractive for the present application;[34] *iii*) these GNPs are relatively uniform and monodisperse;[17] *iv*) The GNP size of 33 nm is greatly larger than that of Pd-Ir NPs (*i.e.*, 6.1 nm), making it convenient to distinguish Pd-Ir NPs from GNPs under electron microscope that is critical for monitoring the heat-induced NP release process.

A film rehydration method, which is widely used for scalable fabrication of liposomes in pharmaceutic industry, was used to fabricate the GVs.[17] Specifically, pristine GVs were prepared

by rehydrating a film of BCP-tethered GNPs in water under sonication, according to our previously published procedures.[17-19] To encapsulate Pd-Ir NPs into GVs, an aqueous suspension of Pd-Ir NPs at a high concentration (~4.5×10^{16} particles/mL) was used for the rehydration process (see details in Supporting Information). As indicated by the TEM and scanning electron microscopy (SEM) images shown in Figure S8a, b, the Pd-Ir NPs@GVs showed an overall spherical shape. The low-magnification SEM image (Figure S8c) demonstrated that the Pd-Ir NPs@GVs could be obtained with a high purity and a good uniformity. Our analyses on 100 random particles indicated that the products had an average diameter of ~400 nm with a standard deviation of 48 nm. As shown by Figure S8d, the vesicular membranes of the GVs were composed of a monolayer of densely packed GNPs, which is consistent with our previous studies.[17,32,35] Based on the packing density and size of GV, the average number of GNPs in an individual GV was roughly estimated to be 339 (Figure S9a). The loading amount of Pd-Ir NPs in individual GVs was estimated to be 1,232 by quantifying elemental Pd and Au in GVs using ICP-OES (see Figure S9b for detailed estimation).

Heat-triggered Release of Pd-Ir NPs. To demonstrate the heat-triggered release of Pd-Ir NPs from GVs, we incubated aqueous suspensions of Pd-Ir NPs@GVs (~0.5 mg/mL in terms of Au element) at different temperatures for 1 hour. The morphological change of samples caused by heat treatment was monitored by TEM and SEM. We found that the assembled GVs gradually collapsed as the temperature increased (Figure 3). Compared to the initial Pd-Ir NPs@GVs (Figure 3a, e), small holes started to appear in the membranes of GVs when the temperature was set to 70 ^{o}C (Figure 3b, f). At 80 ^{o}C, the holes in GVs became more evident and fragments began to fall off of the vesicles (Figure 3c, g). Finally, most of the GVs completely collapsed after 90 ^{o}C treatment (Figure 3d, h). We presume that the dissociation of GNPs is attributed to the breakup of Au-S bonds due to the thermal instability of the bonds at a temperature above 70 ^{o}C.[36,37] The disassembly of GVs is associated with the release of encapsulated Pd-Ir NPs (Figure 3b-d). A number of Pd-Ir NPs can be observed outside the GVs. The heat-triggered release of Pd-Ir NPs is further confirmed by dynamic light scattering (DLS) analysis. Pristine GVs and Pd-Ir NPs were used as control groups. As shown in Figure 4a, after heating at 90 ^{o}C for 1 h, the major size distribution peak of Pd-Ir NPs@GVs suspension shifted from 380 nm (solid, blue) to 260 nm (dashed, blue). In addition, two shoulder peaks at ~8.5 nm and ~32 nm were observed. The 8.5 nm peak matched well with the peak of pristine Pd-Ir NPs (solid, red), indicating the

successful release of Pd-Ir NPs from GVs. The 32 nm peak could be assigned to the dissociated GNPs from GVs since this peak was also observed for pristine GVs after they had been heated (dashed, black). Thermal treatment at 90 ^{o}C for 1 h was adopted for subsequent ELISA experiments. We are aware that heating for 1 h may limit the practical application of the platform for assays. The operation time of assays can be drastically reduced by speeding up the release of payload from GVs *via* the irradiation of near-infrared light or the use of thermoresponsive polymer tethers.[19,33]

Demonstration of Signal Amplification. We also designed a set of experiments to demonstrate the color signal amplification mechanism shown in Figure 1. Briefly, aliquots were taken from an aqueous suspension of Pd-Ir NPs@GVs before and after it had been heated at 90 ^{o}C for 1 h and were employed as catalysts for the oxidation of TMB by H_2O_2. Colored products were quantified by measuring the absorbance at 653 nm ($A_{653\ nm}$), t = 2 min. For comparison, aqueous suspensions of pristine GVs and Pd-Ir NPs with the same amounts of GVs and Pd-Ir NPs (determined by ICP-OES), respectively, as those in Pd-Ir NPs@GVs were also tested. As shown in Figure 4b, before heat treatment, the reaction solution with the presence of Pd-Ir NPs@GVs was nearly colorless with $A_{653\ nm} \approx 0.04$. After heat treatment, the catalytic activity of Pd-Ir NPs@GVs was dramatically enhanced, generating an intense blue color ($A_{653\ nm} = 1.6$, see the inset of Figure 4b). Since almost no absorbance at 653 nm was observed for GVs catalyzed reaction solutions, the enhanced catalytic activity for heat treated Pd-Ir NPs@GVs could be ascribed to the free Pd-Ir NPs released from GVs. It should be mentioned that, before heat treatment, the absorbance of Pd-Ir NPs@GVs catalyzed reaction solution was similar to that of GVs catalyzed reaction solution. This observation demonstrated that the GVs could effectively prevent the leakage of encapsulated Pd-Ir NPs when there is no heating. Based on the values of $A_{653\ nm}$, heat treated Pd-Ir NPs@GVs was as active as pristine Pd-Ir NPs, indicating that most of the Pd-Ir NPs had been released from GVs and their catalytic efficiency was well retained. Taken together, these results clearly demonstrated the signal amplification mechanism described in Figure 1.

Immunoassay of Disease Biomarker. Finally, we applied the Pd-Ir NPs@GVs to ELISA of human prostate surface antigen (PSA), according to the principle shown in Figure 1 (see details in Supporting Information). PSA was chosen because it has been recognized as the key

biomarker responsible for prostate cancer recurrence in patients who have undergone radical prostatectomy.[38] It is vital to detect minute concentrations of PSA at the earliest stage possible to improve the survival rates of those patients.[39,40] Herein, antibodies were conjugated to Pd-Ir NPs@GVs through the EDC/NHS-mediated coupling reaction between the –COOH groups of PAA_{23}-*b*-PS_{250}-S- on GVs and the $–NH_2$ groups on antibodies (see Figure S10).[41,42] PSA standards with a series of concentrations in dilution buffer were monitored in a 96-well microtiter plate (Figure 5a) and quantified using a Perkin Elmer Victor 3 1420 multilabel plate reader. The yellow color of the wells arose from the two-electron oxidation products of TMB (*i.e.*, diimine with $\lambda_{max} \approx 450$ nm) that were formed when the catalytic reaction was quenched by H_2SO_4.[30,43] As shown in Figure 5b, a sigmoid curve regression between the logarithms of absorbance and PSA concentration was obtained. The linear range of detection was found to be 0.2-200 pg/mL with a linear regression value of $r^2 = 0.997$. The coefficient of variations (n = 8) across the entire concentration range were 2.15-12.24%, indicating a good reproducibility of the assay. The limit of detection (defined as the PSA concentration corresponding to a signal that is 3 times the standard deviation above zero calibrator[44,45]) was calculated to be 31 fg/mL. To evaluate the non-specific binding between antibodies conjugated Pd-Ir NPs@GVs and the 96-well microtiter plate/capture antibodies, we have performed a control experiment by excluding antibodies conjugated Pd-Ir NPs@GVs from the blank well (*i.e.*, 0 pg/mL PSA) while keeping all other conditions unchanged. The absorbance at 450 nm for the control group was measured to be 0.024, whereas the absorbance for the blank was 0.036 (both values of absorbance represent the averages from 8 independent measurements). Therefore, on average, the absorbance at 450 nm of each well caused by non-specific binding of antibodies conjugated Pd-Ir NPs@GVs was approximately 0.012. This value is relatively low compared to the absorbance measured from the wells of PSA standards (Figure 5b), suggesting a good specificity of the antibodies conjugated Pd-Ir NPs@GVs.

We benchmarked the Pd-Ir NPs@GVs based ELISA against the conventional HRP based ELISA by using the same set of antibodies and procedures except for the exclusion of heat treatment. Based on the calibration curve shown in Figure S11, the linear detection range and overall coefficient of variations for the HRP based ELISA were found to be 0.2-100 ng/mL and 4.21-14.31%, respectively. The limit of detection was determined to be 48 pg/mL, which was ~1,500-fold higher than our enzyme-free ELISA. This significantly enhanced detection

sensitivity for the enzyme-free ELISA could be attributed to the signal amplification by Pd-Ir NPs@GVs, because other conditions of both ELISAs were kept identical. We also evaluated the correlation between the enzyme-free ELISA with conventional HRP based ELISA by quantifying the same 12 PSA standards of concentrations in 0.5-50 ng/mL using the two ELISAs. For the quantification with enzyme-free ELISA, the standards were diluted with dilution buffer to ensure that the concentrations of PSA were located in the linear range. The final quantitative data was obtained based on the detected PSA concentrations and the dilution factors. As shown in Figure S12, a good correlation between the two ELISAs was found with a correlation coefficient r = 0.998 (n = 12). Taken together, these results demonstrate that our enzyme-free ELISA is three-orders-of-magnitude more sensitive than conventional ELISA, while its reliability and quantitativity are as good as those of conventional ELISA.

To demonstrate the potential application of the Pd-Ir NPs@GVs based ELISA in clinical scenarios, we spiked human plasma samples (from a healthy female donor, provided by the UP Health System-Portage, Houghton, Michigan, United States) with PSA standard at different concentrations in range of 0.4-50 pg/mL and detected the concentrations of PSA. As summarized in Table 1, the analytical recoveries (defined as measured amount of PSA divided by the amount of PSA in original spiked samples[46]) for the four PSA spiked human plasma samples were determined to be in the range of 93.25-105.85%. The coefficient of variation (n = 8) for all samples was below 10.14%. This data implies that the performance of Pd-Ir NPs@GVs based ELISA was not compromised by the complex components in plasma, suggesting the feasibility of this technique in detecting clinical samples.

CONCLUSIONS

In summary, we have demonstrated an enzyme-free signal amplification technique based on Pd-Ir NPs@GVs for colorimetric assay with substantially enhanced detection sensitivity. To the best of our knowledge, such an enzyme-free signal amplification strategy using enzyme-like NPs encapsulated responsive GVs has never been demonstrated elsewhere. The enzyme-free technique we developed can be potentially extended to a variety of other enzymes-based diagnostic technologies beyond ELISA such as immunohistochemistry, western blot, and point-of-care tests. Importantly, this technique is compatible with equipment and procedures of existing sensing technologies, making it practically useful for clinical diagnostics. Further

optimization of the Pd-Ir NPs@GVs system (*e.g.*, size of GV, loading amount of Pd-Ir NPs, particle release time, and catalytic efficiency) and detection of clinical samples are the subjects of our future research.

METHODS

Chemicals and Materials. Sodium hexachloroiridate(III) hydrate ($Na_3IrCl_6 \cdot xH_2O$, MW=473.9), sodium tetrachloropalladate(II) (Na_2PdCl_4, 98%), gold(III) chloride trihydrate ($HAuCl_4 \cdot 3H_2O$, ≥99.9%), potassium bromide (KBr, ≥99%), L-ascorbic acid (AA, ≥99%), poly(vinylpyrrolidone) (PVP, MW≈55,000), 3,3',5,5'-tetramethylbenzidine (TMB, >99%), hydrogen peroxide solution (30 wt. % in H_2O), acetic acid (HOAc, ≥99.7%), sodium acetate (NaOAc, ≥99%), human prostate surface antigen (PSA, ≥99%), Tween 20, bovine serum albumin (BSA, ≥98%), sodium chloride (NaCl, ≥99.5%), potassium chloride (KCl, ≥99%), N-hydroxysulfosuccinimide sodium salt (NHS, ≥98%), N-Ethyl-N′-(3-dimethylaminopropyl)carbodiimide hydrochloride (EDC, ≥99%), sodium phosphate dibasic (Na_2HPO_4, ≥99%), potassium phosphate monobasic (KH_2PO_4, ≥99%), tris base (≥99.9%), sodium citrate, dimethylformamideand (DMF), tetrahydrofuran (THF), sodium azide (NaN_3, ≥99.5%), and sulfuric acid (H_2SO_4, 95-98%) were all obtained from Sigma-Aldrich. Ethylene glycol (EG) was obtained from J. T. Baker. Mouse anti-PSA monoclonal antibody (mouse anti-PSA mAb) and rabbit anti-PSA polyclonal antibody (rabbit anti-PSA pAb) were obtained from Abcam plc. Goat anti-mouse IgG and HRP-goat anti-mouse IgG conjugate were obtained from Thermo Fisher Scientific, Inc.. 96-well microtiter plates (polystyrene, clear, flat bottom) was obtained from Corning Inc.. All aqueous solutions were prepared using deionized (DI) water with a resistivity of 18.0 MΩ·cm.

Preparation of 5.6 nm Pd truncated octahedra to be used as seeds. In a typical synthesis, 30 mL of an EG solution containing 600 mg of PVP was hosted in a glass vial and preheated to 160 °C in an oil bath under magnetic stirring for 10 min. Then, 15 mL of an EG solution containing 240 mg of Na_2PdCl_4 was quickly injected into the reaction solution using a pipette. The reaction was allowed to continue for 3 h. After being washed with acetone once and ethanol twice *via* centrifugation, the final product was re-dispersed in 10 mL of EG for future use. The concentration of Pd element in the final product was determined to be 7.5 mg/mL by ICP-OES, which could be converted to a particle concentration of $\sim 5 \times 10^{15}$ particles/mL (assuming that the particles were perfect octahedra).

Preparation of Pd-Ir core-shell nanoparticles (Pd-Ir NPs). Pd-Ir NPs were prepared by coating a monolayer of Ir on Pd seeds according to our previously published procedure with some modifications.[20] In a standard procedure, 100 mg of PVP and 60 mg of AA were mixed with the 10 mL Pd seeds in EG and were hosted in a 50-mL three-neck flask. The mixture was preheated to 200 °C in an oil bath under

magnetic stirring for 10 min. Then, 8.0 mL of $Na_3IrCl_6 \cdot xH_2O$ solution (7.0 mg/mL, in EG) was injected to the flask at a rate of 1.5 mL/h using a syringe pump. The reaction was allowed to proceed for an additional 10 min after the $Na_3IrCl_6 \cdot xH_2O$ precursor had been completed injected. The products (*i.e.*, Pd-Ir NPs) were collected by centrifugation, washed once with acetone, two times with water, and finally redispersed in 1 mL of DI water for future use. Particle concentration for the suspension of Pd-Ir NPs was estimated to be 4.5×10^{16} by ICP-OES.

Evaluation of peroxidase-like activity. Peroxidase-like activity was measured by the steady-state kinetic assays.[20,24] All assays were carried out at room temperature in 1.0-ml cuvettes (path length, l = 1.0 cm), with 0.2 M NaOAc/HOAc solution, pH 4.0 being used as the reaction buffer. After addition of TMB and H_2O_2 in the buffer system containing nanoparticles as peroxidase mimics, the absorbance of the reaction solution at 653 nm of each sample was immediately measured as a function of time with interval of 6 seconds using a spectrophotometer for 3 min. These "Absorbance *vs.* Time" plots were then used to obtain the slope at the initial point ($Slope_{Initial}$) of each reaction by conducting the first derivation of each curve using OriginPro 9.0 software. The initial reaction velocity (v) was calculated by $Slope_{Initial}$ / ($\varepsilon_{TMB\text{-}653nm} \times l$), where $\varepsilon_{TMB\text{-}653nm}$ is the molar extinction coefficient of TMB at 653 nm that equals 3.9×10^4 $M^{-1}\cdot cm^{-1}$. The plots of v against TMB concentrations ([S]) were fitted using nonlinear regression of the Michaelis-Menten equation. The apparent kinetic parameters K_m and V_{max} were obtained from the double reciprocal plot (or Lineweaver-Burk plot) that was generated from the Michaelis-Menten equation $v = V_{max} \times [S] / (K_m+[S])$,[47] where V_{max} is the maximal reaction velocity and K_m is the Michaelis constant. K_{cat} was derived from $K_{cat} = V_{max}/[E]$, where [E] represents the particle concentration of peroxidase mimics.

Synthesis of amphiphilic block copolymers (BCPs) and gold nanoparticles (GNPs). Amphiphilic BCPs of poly(ethylene oxide)-*b*-polystyrene and poly(acrylic acid)-*b*-polystyrene terminated with a thiol group at polystyrene end (PEO-*b*-PS-SH and PAA-*b*-PS-SH) were synthesized following the reversible addition-fragmentation chain-transfer (RAFT) polymerization procedures reported previously.[17] The BCPs samples were designed with similar polystyrene (PS) lengths (PEO_{45}-*b*-PS_{260}-SH and PAA_{23}-*b*-PS_{250}-SH) as verified by proton nuclear magnetic resonance (^1H NMR) as shown in Figure S7.

GNPs with diameters of 33.0±4.7 nm were prepared by sodium citrate reduction method.[48] Briefly, a 10 mg of $HAuCl_4$ was dissolved in 500 mL H_2O and heated to boiling under stirring. A 3 mL of sodium citrate (1 wt. %) solution was then quickly injected. The reaction mixture was refluxed for 30 min and then used as seeds for further growth of GNPs in the presence of sodium citrate at 80 °C. The resultant 33.0 nm GNPs were collected by centrifugation.

Preparation of gold vesicles (GVs) and Pd-Ir NPs@GVs. GVs and Pd-Ir NPs@GVs were prepared by assembling GNPs tethered with BCPs in the presence of DI water and aqueous suspension of Pd-Ir NPs, respectively, according to our previously reported procedure with minor modifications.

The surface of GNPs was modified with BCPs using the ligand exchange method.[32] A 5 mg BCPs of PEO_{45}-*b*-PS_{260}-SH and PAA_{23}-*b*-PS_{250}-SH with a molar ratio of 20:1 were dissolved in 10 mL DMF. Then, a concentrated solution of GNPs (~2 mg/mL) was slowly added into the BCP solution under vigorous shaking. The mixture was subsequently sonicated for 1 h to avoid the aggregation of GNPs and was then kept static without stirring overnight. The BCP-tethered GNPs were purified by removing free polymers through centrifugation (6-8 times) and were finally redispersed in THF at a concentration of ~0.05 mg/mL.

Self-assembly of BCP-tethered GNPs was conducted by the film rehydration method as reported previously.[19] Briefly, a solution of BCP-modified GNPs in THF was first dried under nitrogen flow to form a thin film on a glass substrate, followed by rehydration in DI water (for pristine GVs) or an aqueous suspension of Pd-Ir NPs at 4.5×10^{16} particles/mL (for Pd-Ir NPs@GVs) with sonication for 1 min. The resultant GVs and Pd-Ir NPs@GVs were collected by centrifugation (5000 rpm, 5 min), washed 8 times with DI water, and finally re-dispersed in water for future use.

Preparation of Pd-Ir NPs@GVs-goat anti-mouse IgG conjugates. Anti-mouse IgG was conjugated to Pd-Ir NPs@GVs using EDC and NHS as coupling agents (see Figure S10).[20,41,42] In brief, 50 μL of Pd-Ir NPs@GVs (~0.5 mg/mL in terms of Au element, in DI water) was added to a 450 μL of 10 mM phosphate buffered saline (PBS, pH 7.4) buffer at room temperature under stirring. Then, 5 μL of EDC (25 mM, in DI water) and 5 μL of NHS (50 mM, in DI water) were added. After 15 min, the particles were washed with DI water twice and redispersed in 50 μL PBS. Subsequently, 50 μL of goat anti-mouse IgG (2 mg/mL, in PBS) was added to the particle suspension. After incubation at room temperature for 30 min, the reaction solution was put in a refrigerator overnight at 4 ^{o}C. Then, 100 μL of blocking solution (5% BSA in PBS) was added to the reaction solution. After 2 h, the final products were collected by centrifugation, washed twice with PBS, and redispersed in 50 μL of PBS containing 1% BSA and 0.05% NaN_3 for future use.

Pd-Ir NPs@GVs-based ELISA of PSA. First, 96-well microtiter plates were coated with rabbit anti-PSA pAb (100 μL per well, 5 μg/mL in carbonate/bicarbonate buffer pH9.6) at 4 ^{o}C overnight. After washing the plates three times with washing buffer (10 mM PBS pH 7.4 containing 0.5% tween 20, PBST), the plates were blocked with 200 μL blocking buffer (3% BSA in PBST) for 2 h at room temperature. The plates were then washed three times with washing buffer, followed by the addition of 100 μL PSA standards or human plasma sample in dilution buffer (1% BSA in PBST). Note that plasma was pre-diluted 2 folds by dilution buffer prior to spiking of PSA and detection. After shaking at room temperature for 2 h, the plates were washed three times with washing buffer, and 100 μL mouse anti-PSA mAb (2 μg/mL, in dilution buffer) was added. After 1 h shake at room temperature, the plates were washed three times, and 100 μL Pd-Ir NPs@GVs-goat anti-mouse IgG conjugates (1:2000, in dilution

buffer) was added, followed by 30 min shake at room temperature. After washing four times, 60 μL DI water was added. After being sealed with a plastic film, the plate was put to an oven set to 90 ^{o}C for 1 h. After the plate had been cooled down to room temperature, 50 μL freshly prepared substrate solution (1.6 mM TMB and 4.0 M H_2O_2 in 0.4 M HOAc/NaOAc buffer, pH 4.0) was added to each well. After 30 min incubation at room temperature, 50 μL of 2 M H_2SO_4 as a stopping solution was added. The absorbance of each well at 450 nm was read using a microplate reader.

The procedure of HRP based ELISA was the same as the Pd-Ir NPs@GVs-based ELISA except for the substitutions of Pd-Ir NPs@GVs-goat anti-mouse IgG conjugates with 100 μL HRP-goat anti-mouse IgG conjugates (1 μg/mL, in dilution buffer), the difference in the components of substrate solution (0.8 mM TMB and 5 mM H_2O_2 in citric acid-Na_2HPO_4 buffer, pH 5.0), and the exclusion of heat treatment step.

Characterizations. The UV-vis spectra were recorded using an Agilent Cary 60 UV-vis spectrophotometer. TEM images were taken using a JEOL JEM-2010 microscope operated at 200 kV. High-resolution TEM (HRTEM) images, high-angle annular dark-field scanning TEM (HAADF-STEM) images and energy dispersive X-ray (EDX) mapping were acquired using a double Cs-corrected JEOL ARM200F TEM at Brookhaven National Laboratory. The concentration of Pd, Ir, and Au ions were determined using an inductively coupled plasma-optical emission spectroscopy (ICP-OES, Perkin Elmer Optima 7000DV), which could be converted to the particle concentration of Pd seeds, Pd-Ir NPs, and Au NPs once the particle sizes and shapes had been resolved by TEM imaging. The X-ray photoelectron spectroscopy (XPS) measurements were performed on an SSX-100 system (Surface Science Laboratories, Inc.) equipped with a monochromated Al Kα X-ray source, a hemispherical sector analyzer (HSA) and a resistive anode detector. X-ray diffraction (XRD) pattern was taken using a Scintag XDS2000 powder diffractometer. Dynamic light scattering (DLS) analysis was conducted using a Photocor-FC light scattering instrument. ^{1}H NMR spectra were recorded with a Bruker AV-400 MHz high-resolution NMR spectrometer in $CDCl_3$. The absorbance of samples in microtiter plates was read using a Perkin Elmer Victor 3 1420 Multilabel Plate Reader. Microtiter plates were shaken using a Corning LSE Digital Microplate Shaker. pH values of buffer solutions were measured using an Oakton pH 700 Benchtop Meter. Photographs of samples in tubes and microplates were taken using a Canon EOS Rebel T5 digital camera.

Conflict of Interest

The authors declare no competing financial interest.

Acknowledgements

This work was supported in part by the National Science Foundation (NSF) Career Award (CHE-1651307) and the startup funds from Michigan Technological University (MTU). Z. Nie gratefully acknowledges the financial support of the NSF Career Award (DMR-1255377). Part of the electron microscopy work at BNL was supported by the U.S. Department of Energy, Basic Energy Sciences, Division of Materials Science and Engineering, under Contract no. DE-AC02-98CH10886. The authors are grateful to Prof. Adrienne Minerick of Department of Chemical Engineering, MTU for her guidance in testing human plasma samples.

Supporting Information Available

Information on materials, experimental details and additional electron microscopy images, spectra, plots, schematics and table is available free of charge *via* the Internet at http://pubs.acs.org.

REFERENCES

1. Price, C. P.; Newman, D. J. *Principles and practice of immunoassay, 2nd ed.*; Stockton: New York, 1997.
2. Wild, D. *The Immunoassay Handbook, 4th ed.*; Elsevier: Amsterdam, 2013.
3. Lequin, R. M. Enzyme Immunoassay (EIA)/Enzyme-Linked Immunosorbent Assay (ELISA). *Clin. Chem.* **2005**, *51*, 2415-2418.
4. Wick, M. R. Histochemistry as a Tool in Morphological Analysis: A Historical Review. *Ann. Diagn. Pathol.* **2012**, *16*, 71-78.
5. Cheng, C.-M.; Martinez, A. W.; Gong, J.; Mace, C. R.; Phillips, S. T.; Carrilho, E.; Mirica, K. A.; Whitesides, G. M. Paper-Based ELISA. *Angew. Chem., Int. Ed.* **2010**, *49*, 4771-4774.
6. Chinen, A. B.; Guan, C. M.; Ferrer, J. R.; Barnaby, S. N.; Merkel, T. J.; Mirkin, C. A. Nanoparticle Probes for the Detection of Cancer Biomarkers, Cells, and Tissues by Fluorescence. *Chem. Rev.* **2015**, *115*, 10530-10574.

7. Tabakman, S. M.; Lau, L.; Robinson, J. T.; Price, J.; Sherlock, S. P.; Wang, H.; Zhang, B.; Chen, Z.; Tangsombatvisit, S.; Jarrell, J. A.; Utz, P. J.; Dai, H. Plasmonic Substrates for Multiplexed Protein Microarrays with Femtomolar Sensitivity and Broad Dynamic Range. *Nat. Commun.* **2011**, *2*, 466.
8. Su, L.-C.; Chen, R.-C.; Li, Y.-C.; Chang, Y.-F.; Lee, Y.-J.; Lee, C.-C.; Chou, C. Detection of Prostate-Specific Antigen with a Paired Surface Plasma Wave Biosensor. *Anal. Chem.* **2010**, *82*, 3714-3718.
9. Soukka, T.; Paukkunen, J.; Härmä, H.; Lönnberg, S.; Lindroos, H.; Lövgren, T. Supersensitive Time-resolved Immunofluorometric Assay of Free Prostate-specific Antigen with Nanoparticle Label Technology. *Clin. Chem.* **2001**, *47*, 1269-1278.
10. Kendall, C.; Ionescu-Matiu, I.; Dreesman, G. R. Utilization of the Biotin/Avidin System to Amplify the Sensitivity of the Enzyme-Linked Immunosorbent Assay (ELISA). *J. Immunol. Methods* **1983**, *56*, 329-339.
11. Leith, A. G.; Griffiths, G. D.; Green, M. A. Quantification of Ricin Toxin Using a Highly Sensitive Avidin/Biotin Enzyme-Linked Immunosorbent Assay. *J. Forensic. Sci. Soc*. **1988**, *28*, 227-236.
12. Gao, Z.; Xu, M.; Hou, L.; Chen, G.; Tang, D. Magnetic Bead-Based Reverse Colorimetric Immunoassay Strategy for Sensing Biomolecules. *Anal. Chem.* **2013**, *85*, 6945-6952.
13. Zhang, Q.; Zhao, B.; Yan, J.; Song, S.; Min, R.; Fan, C. Nanotube-Based Colorimetric Probe for Ultrasensitive Detection of Ataxia Telangiectasia Mutated Protein. *Anal. Chem.* **2011**, *83*, 9191-9196.
14. Ambrosi, A.; Airo, F.; Merkoçi, A. Enhanced Gold Nanoparticle Based ELISA for a Breast Cancer Biomarker. *Anal. Chem.* **2010**, *82*, 1151-1156.
15. Lin, J.; Liu, Y.; Huo, J.; Zhang, A.; Pan, Y.; Bai, H.; Jiao, Z.; Fang, T.; Wang, X.; Cai, Y.; Wang, Q.; Zhang, Y.; Qian, X. Modified Enzyme-Linked Immunosorbent Assay Strategy Using Graphene Oxide Sheets and Gold Nanoparticles Functionalized with Different Antibody Types. *Anal. Chem.* **2013**, *85*, 6228-6232.
16. Liu, D.; Wang, Z.; Jin, A.; Huang, X.; Sun, X.; Wang, F.; Yan, Q.; Ge, S.; Xia, N.; Niu, G.; Hight Walker, A. R.; Chen, X. Acetylcholinesterase-Catalyzed Hydrolysis Allows Ultrasensitive Detection of Pathogens with the Naked Eye. *Angew. Chem., Int. Ed.* **2013**, *52*, 14065-14069.

17. He, J.; Liu, Y.; Babu, T.; Wei, Z.; Nie, Z. Self-Assembly of Inorganic Nanoparticle Vesicles and Tubules Driven by Tethered Linear Block Copolymers. *J. Am. Chem. Soc.* **2012**, *134*, 11342-11345.
18. Huang, P.; Lin, J.; Li, W.; Rong, P. F.; Wang, Z.; Wang, S.; Wang, X.; Sun, X.; Aronova, M.; Niu, G.; Leapman, R. D.; Nie, Z.; Chen, X. Biodegradable Gold Nanovesicles with an Ultrastrong Plasmonic Coupling Effect for Photoacoustic Imaging and Photothermal Therapy. *Angew. Chem., Int. Ed.* **2013**, *52*, 13958-13964.
19. Lin, J.; Wang, S.; Huang, P.; Wang, Z.; Chen, S.; Niu, G.; Li, W.; He, J.; Cui, D.; Lu, G.; Chen, X.; Nie, Z. Photosensitizer-Loaded Gold Vesicles with Strong Plasmonic Coupling Effect for Imaging-Guided Photothermal/Photodynamic Therapy. *ACS Nano* **2013**, *7*, 5320-5329.
20. Xia, X.; Zhang, J.; Lu, N.; Kim, M. J.; Ghale, K.; Xu, Y.; McKenzie, E.; Liu, J.; Ye, H. Pd-Ir Core–Shell Nanocubes: A Type of Highly Efficient and Versatile Peroxidase Mimic. *ACS Nano* **2015**, *9*, 9994-10004.
21. Yang, T.; Ling, H.; Lamonier, J.-F.; Jaroniec, M.; Huang, J.; Monteiro, M. J.; Liu, J. A Synthetic Strategy for Carbon Nanospheres Impregnated with Highly Monodispersed Metal Nanoparticles. *NPG Asia Materials* **2016**, *8*, e240.
22. Liu, J.; Hartono, S. B.; Liu, T.; Kantharidis, P.; Middelberg, A. P. J.; Lu, G. X.; He, L.; Qiao, S. Z. Magnetic Silica Spheres with Large Nanopores for Nucleic Acid Adsorption and Cellular Uptake. *Biomaterials* **2012**, *33*, 970-978.
23. Mani, V.; Chikkaveeraiah, B. V.; Patel, V.; Gutkind, J. S.; Rusling, J. F. Ultrasensitive Immunosensor for Cancer Biomarker Proteins Using Gold Nanoparticle Film Electrodes and Multienzyme-particle Amplification. *ACS Nano* **2009**, *3*, 585-594.
24. Qian, J.; Zhang, C.; Cao, X.; Liu, S. Versatile Immunosensor Using a Quantum Dot Coated Silica Nanosphere as a Label for Signal Amplification. *Anal. Chem.* **2010**, *82*, 6422-6429.
25. Grinyte, R.; Barroso, J.; Möller, M.; Saa, L.; Pavlov, V. Microbead QD-ELISA: Microbead ELISA Using Biocatalytic Formation of Quantum Dots for Ultra High Sensitive Optical and Electrochemical Detection. *ACS Appl. Mater. Interfaces* **2016**, *8*, 29252-29260.
26. Xia, X.; Figueroa-Cosme, L.; Tao, J.; Peng, H.-C.; Niu, G.; Zhu, Y.; Xia, Y. Facile Synthesis of Iridium Nanocrystals with Well-Controlled Facets Using Seed-Mediated Growth. *J. Am. Chem. Soc.* **2014**, *136*, 10878-10881.

27. Arblaster, J. W. Crystallographic Properties of Iridium. *Platinum Metals Rev.* **2010**, *54*, 93-102.
28. Habas, S. E.; Lee, H.; Radmilovic, V.; Somorjai, G. A.; Yang, P. Shaping Binary Metal Nanocrystals Through Epitaxial Seeded Growth. *Nat. Mater.* **2007**, *6*, 692-697.
29. Gao, L.; Zhuang, J.; Nie, L.; Zhang, J.; Zhang, Y.; Gu, N.; Wang, T.; Feng, J.; Yang, D.; Perrett, S.; Yan, X. Intrinsic Peroxidase-like Activity of Ferromagnetic Nanoparticles. *Nat. Nanotechnol.* **2007**, *2*, 577-583.
30. Josephy, P. D.; Eling, T.; Mason, R. P. The Horseradish Peroxidase-Catalyzed Oxidation of 3,5,3',5'-Tetramethylbenzidine. Free Radical and Charge-Transfer Complex Intermediates. *J. Biol. Chem.* **1982**, *257*, 3669-3675.
31. Frey, A.; Meckelein, B.; Externest, D.; Schmidt, M. A. A Stable and Highly Sensitive 3,5,3',5'-Tetramethylbenzidine-Based Substrate Reagent for Enzyme-Linked Immunosorbent Assays. *J. Immunol. Methods* **2000**, *233*, 47-56.
32. He, J.; Huang, X.; Li, Y.-C.; Liu, Y.; Babu, T.; Aronova, M. A.; Wang, S.; Lu, Z.; Chen, X.; Nie, Z. Self-Assembly of Amphiphilic Plasmonic Micelle-Like Nanoparticles in Selective Solvents. *J. Am. Chem. Soc.* **2013**, *135*, 7974-7984.
33. He, J.; Wei, Z.; Wang, L.; Tomova, Z.; Babu, T.; Wang, C.; Han, X.; Fourkas, J. T.; Nie, Z. Hydrodynamically Driven Self-Assembly of Giant Vesicles of Metal Nanoparticles for Remote-Controlled Release. *Angew. Chem., Int. Ed.* **2013**, *52*, 2463-2468.
34. Anajafi, T.; Mallik, S. Polymersome-Based Drug-Delivery Strategies for Cancer Therapeutics. *Ther. Deliv.* **2015**, *6*, 521-534.
35. Liu, J.; Li, Y.; He, J.; Duelge, K. J.; Lu, Z.; Nie, Z. Entropy-Driven Pattern Formation of Hybrid Vesicular Assemblies Made from Molecular and Nanoparticle Amphiphiles. *J. Am. Chem. Soc.* **2014**, *136*, 2602-2610.
36. Bhatt, N.; Huang, P. J.; Dave, N.; Liu, J. Dissociation and Degradation of Thiol-Modified DNA on Gold Nanoparticles in Aqueous and Organic Solvents. *Langmuir* **2011**, *27*, 6132-6137.
37. Li, F.; Zhang, H.; Dever, B.; Li, X.-F.; Le, X. C. Thermal Stability of DNA Functionalized Gold Nanoparticles. *Bioconjugate Chem.* **2013**, *24*, 1790-1797.
38. Rissin, D. M.; Kan, C. W.; Campbell, T. G.; Howes, S. C.; Fournier, D. R.; Song, L.; Piech, T.; Patel, P. P.; Chang, L.; Rivnak, A. J.; Ferrell, E. P.; Randall, J. D.; Provuncher, G. K.; Walt,

D. R.; Duffy, D. C. Single-Molecule Enzyme-Linked Immunosorbent Assay Detects Serum Proteins at Subfemtomolar Concentrations. *Nat. Biotechnol.* **2010**, *28*, 595-599.

39. Laxman, B.; Morris, D. S.; Yu, J.; Siddiqui, J.; Cao, J.; Mehra, R.; Lonigro, R. J.; Tsodikov, A.; Wei, J. T.; Tomlins, S. A.; Chinnaiyan, A. M. A First-Generation Multiplex Biomarker Analysis of Urine for the Early Detection of Prostate Cancer. *Cancer Res.* **2008**, *68*, 645-649.
40. Rica, R.; Stevens, M. M. Plasmonic ELISA for the Ultrasensitive Detection of Disease Biomarkers with the Naked Eye. *Nat. Nanotechnol.* **2012**, *7*, 821-824.
41. Qian, X.; Peng, X.-H.; Ansari, D. O.; Yin-Goen, Q.; Chen, G. Z.; Shin, D. M.; Yang, L.; Young, A. N.; Wang, M.; Nie, S. *In Vivo* Tumor Targeting and Spectroscopic Detection with Surface-Enhanced Raman Nanoparticle Tags. *Nat. Biotechnol.* **2008**, *26*, 83-90.
42. Hermanson, G. T. *Bioconjugate Techniques*; Academic Press: San Diego, CA, **1996**.
43. Stefan, L.; Denat, F.; Monchaud, D. Insights into How Nucleotide Supplements Enhance the Peroxidase-Mimicking DNAzyme Activity of the G-Quadruplex/Hemin System. *Nucleic Acids Res.* **2012**, *40*, 8759-8772.
44. Armbruster, D. A.; Tillman, M. D.; Hubbs, L. M. Limit of Detection (LQD)/Limit of Quantitation (LOQ): Comparison of the Empirical and the Statistical Methods Exemplified with GC-MS Assays of Abused Drugs. *Clin. Chem.* **1994**, *40*, 1233-1238.
45. Armbruster, D. A.; Pry, T. Limit of Blank, Limit of Detection and Limit of Quantitation. *Clin. Biochem. Rev.* **2008**, *29*, S49-S52.
46. Burns, D. T.; Danzer, K.; Townshend, A. Use of the Term "Recovery" and "Apparent Recovery" in Analytical Procedures. *Pure Appl. Chem.* **2002**, *74*, 2201-2205.
47. Lineweaver, H.; Burk, D. The Determination of Enzyme Dissociation Constants. *J. Am. Chem. Soc.* **1934**, *56*, 658-666.
48. Frens, G. Controlled Nucleation for the Regulation of the Particle Size in Monodisperse Gold Suspensions. *Nature-Phys. Sci.* **1973**, *241*, 20-22.

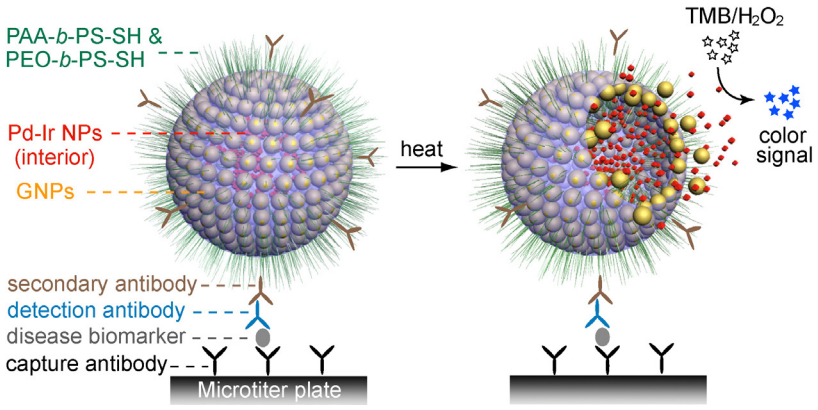

Figure 1. Schematic illustration of utilizing Pd-Ir NPs@GVs based ELISA for detection of disease biomarkers. The Pd-Ir NPs released from captured GVs act as effective peroxidase mimics to catalyze chromogenic substrates.

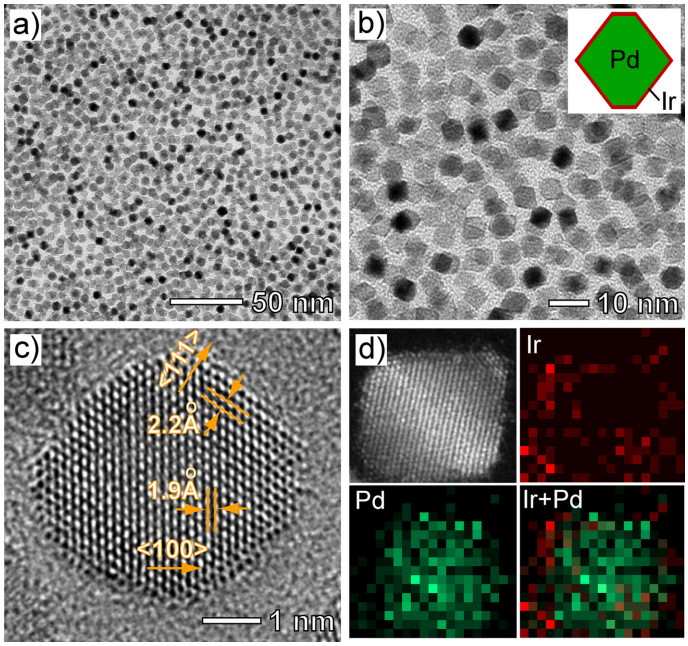

Figure 2. Structural and compositional analyses of Pd-Ir NPs prepared by depositing Ir atoms on 5.6 nm Pd truncated octahedral seeds. (a,b) low (a) and high (b) magnification TEM image of Pd-Ir NPs. The inset is a 2D schematic model. (c) HRTEM image of an individual Pd-Ir NP; (d) HAADF-STEM image and EDX mapping of an individual Pd-Ir NP (red = Ir, green = Pd).

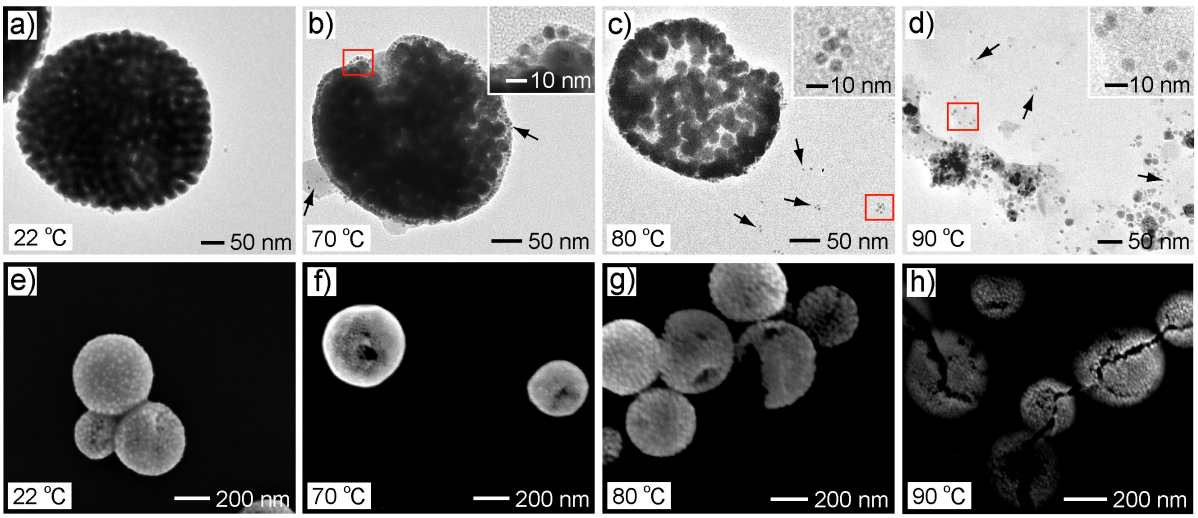

Figure 3. Heat-triggered release of Pd-Ir NPs from GVs. Representative (a-d) TEM and (e-h) SEM images of the Pd-Ir NPs@GVs treated at different temperatures (marked in each image) for 1 h. In (b-d), insets show magnified TEM images of corresponding regions marked by red boxes. Some of the released Pd-Ir NPs are indicated by black arrows.

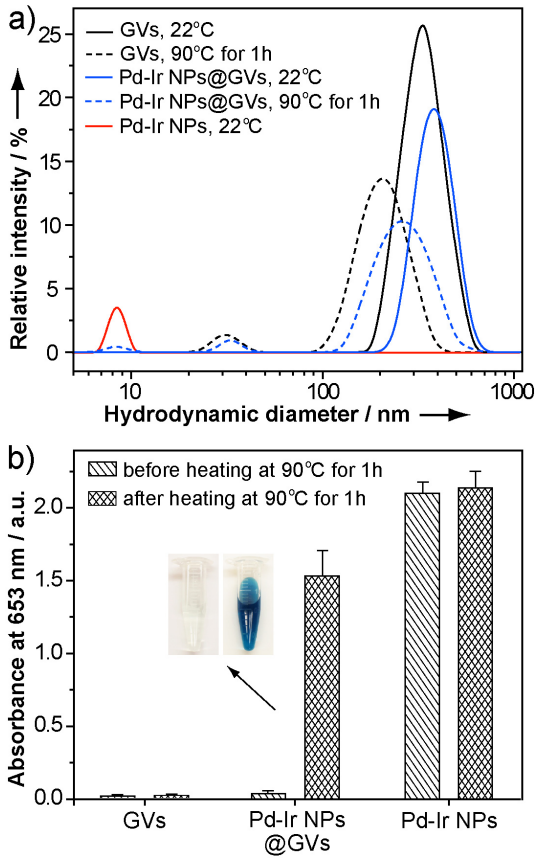

Figure 4. Comparison of the properties of Pd-Ir NPs@GVs before and after heat treatment (90 °C, 1 h). (a) DLS analysis of different samples: GVs (black), Pd-Ir NPs@GVs (blue), and Pd-Ir NPs (red); (b) Absorbance at 653 nm measured from catalytic reaction solutions containing different particles (marked under the bars) at t = 2 min. Concentrations of GVs were kept the same for suspensions of GVs and Pd-Ir NPs@GVs, while the concentrations of Pd-Ir NPs were kept the same for suspensions of Pd-Ir NPs@GVs and Pd-Ir NPs. Inset shows photographs of reaction solutions corresponding to Pd-Ir NPs@GVs. All tests in (a) and (b) were conducted at room temperature (~22 °C).

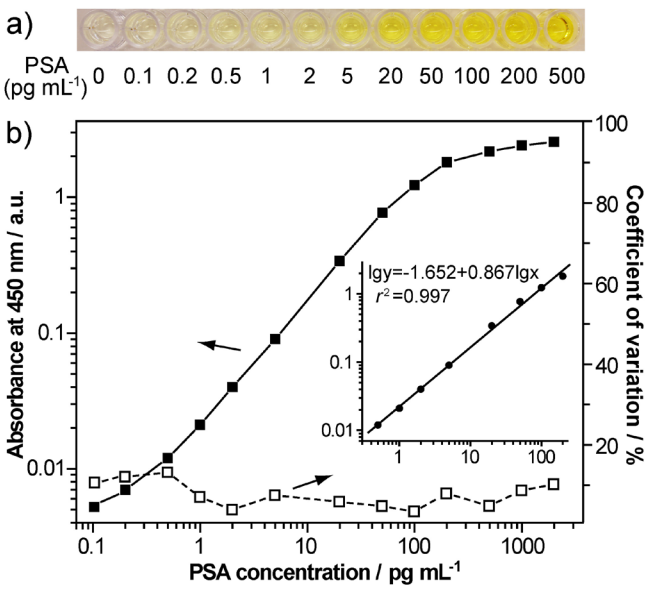

Figure 5. Pd-Ir NPs@GVs based ELISA of PSA. (a) Representative photographs taken from the ELISA of PSA standards; (b) Corresponding calibration curve (■) and imprecision profile (□) of the detection results shown in (a). Note that absorbance of the blank (*i.e.*, 0 pg/mL PSA) was subtracted from those of PSA standards. Inset shows the linear range region of the calibration curve. All the data points represent the averages from 8 independent measurements.

Table 1. Analytical recoveries of Pd-Ir NPs@GVs based ELISA in detecting PSA spiked human plasma samples.

PSA amount spiked (pg/mL)	PSA amount measured (pg/mL)	Coefficient of variations (%, n = 8)	Relative errors (%)	Recovery (%)
0.40	0.37	10.14	-6.75	93.25
2.00	2.12	7.71	5.85	105.85
10.00	9.87	3.92	-1.28	98.72
50.00	51.71	6.85	3.41	103.41